

# Epitaxial Growth of Hexagonal BaNiO<sub>3-δ</sub> Thin Films on SrTiO<sub>3</sub> (111) Substrates

Binod Paudel<sup>1</sup>, Krishna P. Koirala<sup>1</sup>, Le Wang<sup>1,\*</sup>, Zengqing Zhuo<sup>2</sup>, Mark E. Bowden<sup>3</sup>, Peter V. Sushko<sup>1</sup>, Wanli Yang<sup>2</sup>, George E. Sterbinsky<sup>4</sup>, Scott A. Chambers<sup>1</sup>, Tiffany C. Kaspar<sup>1,\*</sup>, Yingge Du<sup>1</sup>

<sup>1</sup>Physical and Computational Sciences Directorate, Pacific Northwest National Laboratory, Richland, WA 99354, USA

<sup>2</sup>Advanced Light Source, Lawrence Berkeley National Laboratory, Berkeley, CA 94720, USA

<sup>3</sup>Environmental Molecular Sciences Laboratory, Pacific Northwest National Laboratory, Richland, WA 99354, USA

<sup>4</sup>Advanced Photon Source, Argonne National Laboratory, Lemont, IL 60439, USA

\* Authors to whom correspondence should be addressed: [le.wang@pnnl.gov](mailto:le.wang@pnnl.gov), [tiffany.kaspar@pnnl.gov](mailto:tiffany.kaspar@pnnl.gov)

## Abstract:

Transition metal oxides containing Ni species in oxidation states higher than 3+ often exhibit high catalytic activity, which makes them promising for applications as advanced electrocatalysts for water splitting and fuel cells. Here, we examine the structure and properties of BaNiO<sub>3</sub> (BNO) thin films, containing formally Ni<sup>4+</sup>, grown on SrTiO<sub>3</sub>(111) substrates using oxygen-plasma-assisted molecular beam epitaxy. X-ray diffraction and scanning transmission electron microscopy measurements reveal that BNO films have a hexagonal structure with *c*- and *a*-axis mixed textures showing epitaxial relationships BNO(0001)∥SrTiO<sub>3</sub>(111) and BNO(10 $\bar{1}$ 0)∥SrTiO<sub>3</sub>(111), respectively. The formation of *a*-axis texture is dominant due to the smaller lattice mismatch with the substrate. Density functional theory calculations confirm that the hexagonal BNO film with *a*-axis texture is energetically more favorable than the competing *c*-axis texture. Detailed spectroscopy data analysis indicates that hexagonal BNO films contain mixtures of Ni<sup>2+</sup>, Ni<sup>3+</sup>, and Ni<sup>4+</sup> species, with Ni<sup>4+</sup> being dominant. Our study provides insights into stabilizing Ni<sup>4+</sup> in complex oxides, important for further exploration of the potential of materials containing Ni<sup>4+</sup>.

**Keywords:** nickelates, BaNiO<sub>3</sub>, thin film epitaxy, high-valence Ni, lattice mismatch

## Introduction

ABO<sub>3</sub>-type perovskite rare earth nickelates RNiO<sub>3</sub> (where *R* denotes lanthanide) are an extensively investigated family of complex oxides due to their rich phase diagrams. [1–3] This oxide family demonstrates exotic physical properties, such as metal-insulator transitions (MIT), [4] charge ordering, [5] unusual magnetic ordering, [6] and colossal resistive switching. [7,8] Integration of nickelates into heterostructures through thin film epitaxy can induce orbital degeneracy breaking and quantum confinement effects that effectively modulate their functional properties. [2,9,10] The sensitivity of nickelates to the details of the structure and composition is made evident by the fact that superconductivity was only observed in the reduced R<sub>1-x</sub>Sr<sub>x</sub>NiO<sub>2</sub> and R<sub>1-x</sub>Ca<sub>x</sub>NiO<sub>2</sub> epitaxial thin films, [11–14] whereas it is absent in the bulk R<sub>1-x</sub>Sr<sub>x</sub>NiO<sub>2</sub>. [15,16]

Recently, nickelates have also garnered special attention in catalysis because of their excellent electrocatalytic performance, [17–20] which can be attributed to the small or negative charge transfer energy ( $\Delta$ ) defined as the difference between the Ni 3d band and O 2p band edge (negative  $\Delta$  corresponds to Ni 3d band below the O 2p band maximum) that results in strong Ni 3d-O 2p hybridization. [21] Hole doping in RNiO<sub>3</sub> can push the Ni formal valence above 3+, [22] which can further increase the extent of Ni 3d-O 2p hybridization, [19] thereby promoting an enhancement in the electrocatalytic activity. [18,20] However, it has been shown that the synthesis of parent perovskite-phases R<sub>1-x</sub>Sr<sub>x</sub>NiO<sub>3</sub> and R<sub>1-x</sub>Ca<sub>x</sub>NiO<sub>3</sub> in the form of thin films is challenging due to instability of the high-valence Ni species. [22–25] Phase segregation was observed when attempting to deposit SrNiO<sub>3- $\delta$</sub>  (SNO) on (001)-oriented perovskite-like single

crystal substrates using oxygen-plasma-assisted molecular beam epitaxy (OPA-MBE). [26,27] Two coexisting oxygen-deficient Ruddlesden-Popper phases,  $\text{Sr}_2\text{NiO}_3$  and  $\text{SrNi}_2\text{O}_3$ , formed instead, and Ni ions were stabilized in the energetically preferred  $\text{Ni}^{2+}$  state. [26] Previous studies reported the formation of single-u.c. SNO in superlattices with  $\text{LaFeO}_3$  and  $\text{SrTiO}_3$  (STO). [27,28] However, the instability of SNO in the top layer of these superlattices limits exploration of the impact of  $\text{Ni}^{4+}$  on the mechanisms and characteristics of electrocatalytic reactions that occur primarily at the surface.

Bulk SNO is expected to form a hexagonal structure with a face-shared arrangement of  $\text{NiO}_6$  octahedra because its tolerance factor ( $t$ ) is larger than unity. [29] Due to the high Gibbs formation energy of  $\text{Ni}^{4+}$ , [30] there has been very limited success in the synthesis of bulk hexagonal-structured SNO until recently. [31,32] Replacement of Sr with larger size Ba can stabilize hexagonal closest packing. [32] Thus, bulk hexagonal-structured  $\text{BaNiO}_3$  (BNO) has been successfully synthesized by several groups. [18,33–38] However, the successful synthesis of BNO epitaxial thin films has not yet been reported.

In our investigation, we used density functional theory (DFT) simulations to evaluate the phase stability of BNO thin films on (111)-oriented perovskite single crystal substrates. We found that hexagonal BNO thin films are energetically more stable than those in the cubic perovskite phase when deposited on substrates with lattice parameters ranging from 3.8 to 4.1 Å. Experimentally, we observed that hexagonal phase BNO thin films with  $c$ - and  $a$ -axis mixed textures are stabilized on STO(111) substrates. The  $a$ -axis texture,  $\text{BNO}(10\bar{1}0)/\text{STO}(111)$ , is energetically more favorable due to the smaller lattice mismatch with the substrate compared to the  $c$ -axis texture,  $\text{BNO}(0001)/\text{STO}(111)$ . X-ray photoelectron spectroscopy (XPS) and X-ray

absorption spectroscopy (XAS) measurements revealed that the Ni valence in BNO films includes mixtures of Ni<sup>2+</sup>, Ni<sup>3+</sup>, and Ni<sup>4+</sup> with Ni<sup>4+</sup> being dominant.

## Results and Discussion

To prepare the STO substrate, we employed a wet etching method similar to that described elsewhere.[39] BNO films were grown on STO(111) substrates by OPA-MBE. Ba and Ni were evaporated from effusion cells, and their evaporation rates were calibrated using a quartz crystal microbalance prior to the growth. The substrate temperature was maintained at 650 °C, and the activated oxygen partial pressure was kept at  $\sim 5 \times 10^{-6}$  Torr throughout the growth process. To prevent the oxygen vacancy formation in BNO films, an alternating deposition and annealing approach was employed, as described in our previous work. [23] *In situ* reflection high-energy electron diffraction (RHEED) was used to monitor the overall growth process (Figure S1). After the growth, the samples were gradually cooled down in an activated oxygen atmosphere at a chamber pressure of  $\sim 2 \times 10^{-5}$  Torr. The temperature was ramped down from 650 to 500 °C at a rate of 25 °C/min, followed by a one-hour annealing step at 500 °C. Subsequently, a second ramp was performed from 500 to 200 °C at a rate of 5 °C/min, followed by a two-hour annealing step at 250 °C. Finally, the samples were cooled down to room temperature at a rate of 1 °C/min. [40,41] High-resolution out-of-plane X-ray diffraction (XRD)  $\theta$ - $2\theta$  scan (Figure 1a) reveals two well-defined families of peaks ( $\{h0\bar{h}0\}$ ,  $h = 1, 2, 3, 4$ ) and ( $\{000l\}$ ,  $l = 2, 4$ ), indicating that the BNO film nucleates with both *a*- and *c*-axis textures. The simulations (Figure S2) clearly show the overlap of the (20 $\bar{2}$ 0) and (40 $\bar{4}$ 0) *a*-axis peaks with the (0002) and (0004) *c*-axis peaks, respectively. To examine the film's symmetry and epitaxial relationships, two off-axis phi-scans were performed along the film (22 $\bar{4}$ 0) and (10 $\bar{1}$ 3) reflections, and along the substrate (112) reflection, as shown in Figure 1b. The STO(112) phi scan shows three peaks

separated by  $120^\circ$ , corresponding to the threefold triangular surface symmetry of the STO(111) substrate. A phi scan was performed to probe the in-plane orientation of the  $c$ -axis texture by measuring the BNO  $(10\bar{1}3)$  reflection at an appropriate  $\chi$  angle. The alignment between the six BNO features and the three STO peaks confirms the six-fold rotational symmetry of hexagonal  $c$ -axis BNO, which directly grows on the in-plane triangular STO(111) surface with an epitaxial relationship of BNO(0001)  $[10\bar{1}0] \parallel$  STO(111)  $[11\bar{2}]$ . Likewise, the in-plane orientation of the  $a$ -axis texture was determined with another phi-scan of the BNO(22 $\bar{4}$ 0) reflection at an appropriate  $\chi$  angle, which reveals the epitaxial relationship BNO(10 $\bar{1}$ 0)  $[0001] \parallel$  STO(111)  $[11\bar{2}]$ . The  $30^\circ$  offset between the two BNO phi scans is a consequence of the observed epitaxial relationships and the selection of particular reflections for the phi scans. The six observed BNO peaks indicate the overall six-fold rotational symmetry of the  $a$ -axis texture, which arises from the three in-plane tetragonal BNO domains rotated by  $120^\circ$ , as depicted in Figure S3a. Reciprocal space mapping (RSM) (Figure S3c) reveals that the BNO film was partially relaxed.

Additional structural information on the BNO film was obtained using high angle annular dark field-scanning transmission electron microscopy (HAADF-STEM). Figure 1c shows an atomic-resolution HAADF-STEM image of the BNO/STO heterostructure viewed along STO  $\langle 11\bar{2} \rangle$  direction. An interfacial transition region (marked by arrow and extensively described in Figure S4) was observed at the BNO/STO interface. Beyond the interfacial transition region, the  $a$ -axis texture of hexagonal phase BNO (see schematic in Figure 1d) was clearly observed in the left side of the STEM image, as confirmed by the Fast Fourier Transform (FFT) patterns (Figure 1e). In addition, we observed a lattice structure with a slightly different appearance on the right side of the STEM image (marked by yellow colored rectangle). FFT patterns (Figure 1f) in this region perfectly match those (Figure 1e) on the left side of the STEM image, suggesting that it is

not related to the *c*-axis texture, but to be the *a*-axis texture. To further validate our findings, we rotated the simulated STEM-HAADF image of the *a*-axis texture by up to 2 degrees (Figure S5). And the results showed a strong correspondence with the STEM-HAADF image. The distortions on the hexagonal lattice are likely due to the compressive and tensile strains along the in-plane and out of plane directions, respectively. The *c*-axis texture detected in XRD experiments was not observed in the HAADF-STEM images. To verify its presence, we have performed a  $\phi$ -scan for a peak inclined to the (0001) planes and found it at the anticipated *d*-spacing and inclination angle (Figure 1b). Since the (0001) and ( $h0\bar{h}0$ ) peaks locate closely when  $l = h$ , resolution of the out-of-plane  $\theta$ - $2\theta$  scan is not sufficient to estimate the volume fractions corresponding to these different orientations. However, at high diffraction angles where the peaks are better resolved, it appears that the (0001) orientation is considerably less abundant. Consequently, the probability of lifting out a region of (0001)-oriented BNO for STEM imaging is quite low and we identified only ( $h0\bar{h}0$ ) orientation in the FIB sections we imaged.

In order to understand why both *a*- and *c*-axis textures were formed during h-BNO growth, we examined the dependence of their potential energies on the strain imposed by a cubic perovskite lattice terminated with (111) plane. In both cases, we varied the perovskite lattice constant and recalculated the in-plane vectors of the supercells representing the *a*- and *c*-axis textures accordingly. The internal atomic coordinates and the supercell vectors in the out-of-plane direction were fully relaxed. Similar calculations were performed for the perovskite BNO simulated as a continuation of the STO(111) substrate. The supercells for strained perovskite and hexagonal BNO on STO(111) are shown in Figure S6. Figure 2 shows the crystal structure orientations of *a*- and *c*-axis textures as viewed along the STO  $\langle 111 \rangle$  direction and strain energy comparisons among the two h-BNO textures and perovskite BNO. The *c*-axis texture is under an

identical compressive biaxial lattice mismatch of  $\sim 1.93\%$  in both in-plane directions along  $\text{BNO}[11\bar{2}0]\parallel\text{STO}[\bar{1}10]$  and  $\text{BNO}[10\bar{1}0]\parallel\text{STO}[11\bar{2}]$ , as shown in Figure 2a. On the other hand, compressive mismatches of  $\sim 1.93\%$  and  $\sim 0.6\%$  have been observed along the  $\text{BNO}[11\bar{2}0]\parallel\text{STO}[\bar{1}10]$  and  $\text{BNO}[0001]\parallel\text{STO}[11\bar{2}]$  directions, respectively, for the  $a$ -axis texture (Figure 2b). The smaller lattice mismatch in the  $a$ -axis texture along  $\text{BNO}[0001]\parallel\text{STO}[11\bar{2}]$  is observed due to a coincidence lattice match with the  $30^\circ$ -rotated  $\text{STO}(111)$  in-plane lattice constant, i.e.,  $\sqrt{6}a_{\text{STO}}$  ( $a_{\text{STO}} = 3.905 \text{ \AA}$ ,  $\sqrt{6}a_{\text{STO}} = 9.57 \text{ \AA}$ ) with  $2c_{\text{BNO}}$  ( $c_{\text{BNO}} = 4.81 \text{ \AA}$ ,  $2c_{\text{BNO}} = 9.62 \text{ \AA}$ ). The calculated energy minimum for the  $a$ -axis texture falls at a smaller lattice constant than that of the  $c$ -axis texture due to their unique strains, as shown in Figure 3c. The  $a$ -axis texture has its minimum energy at  $a_{\text{Sub}} = 5.57 \text{ \AA}$ , while the  $c$ -axis texture has an energy minimum when  $a_{\text{Sub}}$  equals the bulk lattice parameter of BNO i.e.,  $5.63 \text{ \AA}$ . For the  $\text{STO}(111)$  substrates, the strain energy required for  $a$ -axis textured BNO is  $25 \text{ meV}$  lower per formula unit than for its  $c$ -axis counterpart, indicating that the  $a$ -axis texture is the most energetically favorable configuration. For comparison, the perovskite  $\text{BNO}(111)/\text{STO}(111)$  configuration is significantly less favorable (by  $\sim 1.3 \text{ eV}$  per f.u.) than either  $c$ -axis or  $a$ -axis textures, indicating that perovskite BNO is unlikely to nucleate. These calculations are consistent with experimental results that the formation of mixed textures in the h-BNO film is possible; this co-existence of the two phases is attributed to the small difference in their stability at the epitaxial strains imposed by the  $\text{STO}(111)$  substrate. In addition, based on our DFT simulations (Figure 2c), both textures are sensitive to strain which, therefore, can be utilized to favor preferential formation of one texture over another. While the potential energy minima for these textures are relatively close to each other, the quadratic dependence of the potential energy on the lattice parameter ensures that the energy difference between these phases increases at least linearly with increasing tensile or

compressive strain. Specifically, for the LaAlO<sub>3</sub> substrate (lattice parameter ~5.36 Å), the energy difference between textures is expected to triple that found for the SrTiO<sub>3</sub> substrate, thus highly increasing the likelihood of achieving a single-phase *a*-axis texture of *h*-BNO film. Conversely, employing a single crystal substrate with a large lattice constant, e.g., KTaO<sub>3</sub> (lattice parameter ~5.64 Å) will switch the texture prevalence from *a*-axis to *c*-axis, even if marginally so.

To identify the Ni valence in BNO, we conducted *in situ* XPS along with *ex situ* *L*- and *K*-edge XAS measurements. The reference spectra for Ni<sup>3+</sup> and Ni<sup>2+</sup> were measured using an oxygen plasma annealed NdNiO<sub>3</sub> (NNO) film and a NiO film, respectively.[26] Ni 2p and 3p XPS spectra are shifted so that the corresponding O 1s peak falls at 530.0 eV. As shown in Figure 3a, the Ni 2p line shapes for BNO show a clear distinction from the Ni<sup>3+</sup> and Ni<sup>2+</sup> reference spectra. The Ni 2p<sub>3/2</sub> main feature peak for BNO (marked by blue dashed line) is shifted to higher binding energy relative to that of NNO, suggesting that the Ni valence in BNO should be higher than 3+. Based on the chemical shift (~2 eV) of the Ni 2p<sub>3/2</sub> peak relative to the Ni 2p peak of NNO, we speculate that the Ni valence in BNO is dominated by Ni<sup>4+</sup>. Additionally, a shoulder located at the lower binding energy side is also observed in the Ni 2p<sub>3/2</sub> feature for BNO, indicating the presence of mixed Ni valence in BNO. The Ni 2p<sub>3/2</sub> shoulder feature peak energy is the same as that of NNO, suggesting that the Ni valence in BNO includes Ni<sup>3+</sup>. The Ni valence assignment (a mixture of Ni<sup>4+</sup> and Ni<sup>3+</sup>) from Ni 2p XPS is consistent with Ni 3p XPS (Figure S7a) and corroborated by XAS measurements collected at the Ni *K*-edge (Figure S7b) and the Ni *L*-edge. Figure 3b shows the total electron yield (TEY) mode Ni *L*-edge spectra for BNO, along with that of Ni<sup>3+</sup> and Ni<sup>2+</sup> references. The main feature peaks at *L*<sub>2,3</sub> edges shift towards higher photon energy compared to the Ni<sup>3+</sup> reference, indicating that the dominant formal Ni valence in BNO should be higher than Ni<sup>3+</sup>. The measured energy shift (~1.5

eV) of the Ni  $L$ -edges relative to that in NNO suggests that the dominant Ni valence in BNO is  $\text{Ni}^{4+}$ , [42] consistent with our XPS analysis. Moreover, the shoulders (observed at lower photon energy side) of both  $L_3$  and  $L_2$  edges match the peak positions of  $\text{Ni}^{2+}$  and  $\text{Ni}^{3+}$  reference spectra, confirming the presence of a mix of  $\text{Ni}^{4+}$ ,  $\text{Ni}^{3+}$ , and  $\text{Ni}^{2+}$  in BNO. In contrast to XPS, which mainly detects the near surface (the effective attenuation length of XPS is  $\sim 5$  nm), [43] XAS (the attenuation length of TEY mode is  $> 10$  nm) [44] can probe deeper. Thus, we conclude that the  $\text{Ni}^{2+}$  feature, observed in Ni  $L$ -edge XAS but mostly absent in Ni 2p XPS, could be ascribed to the contribution from the region close to the interface. This is confirmed by our STEM measurements (Figure S8) which capture NiO secondary phases close to the interfacial regions. The existence of the insulating NiO secondary phases in BNO films can strongly affect the in-plane electrical transport behavior. These secondary phases might be responsible for the observed insulating behavior manifested by high resistivity of  $2.1 \times 10^2 \Omega \cdot \text{cm}$  at 300 K, as shown in Figure 3d. In contrast, NNO shows metallic behavior with resistivity of only  $\sim 3.2 \times 10^{-4} \Omega \cdot \text{cm}$  at 300 K. [26]

The valence states of transition metals (TMs) in oxides can also be qualitatively assessed by the pre-edge spectral feature at the O  $K$ -edge. For the same TM, a lower O  $K$  pre-edge peak energy corresponds to a higher TM valence state. [45] Moreover, a higher intensity of the O  $K$  pre-edge peak suggests stronger TM 3d and O 2p hybridization. We compared the O  $K$  pre-edge feature of BNO with the reference spectra of NNO and NiO. As shown in Figure 3c, the O  $K$  pre-edge feature peak of BNO falls at the same position ( $\sim 528$  eV) as that of NNO, suggesting that the Ni valence in BNO is close to  $\text{Ni}^{3+}$ . Compared to NNO, the higher O  $K$  pre-edge peak intensity of BNO indicates stronger Ni 3d-O 2p hybridization, which can be ascribed to the contribution from  $\text{Ni}^{4+}$  (we should note that the O  $K$  pre-edge feature peak position of  $\text{Ni}^{4+}$  is

very close to that of Ni<sup>3+</sup>) [19,45]. Moreover, the coincidence of a small feature at ~ 532 eV with the O *K* pre-edge feature peak of NiO also implies the presence of Ni<sup>2+</sup> in BNO, in agreement with the Ni *L*-edge XAS measurements.

## Summary

In summary, we have synthesized BNO thin films on (111)-oriented STO substrates by OPA-MBE. Our XRD and STEM studies demonstrate that BNO films can be stabilized in the hexagonal phase with *a*- and *c*-axis mixed textures and thus display epitaxial relationships of BNO(10 $\bar{1}$ 0) [0001]||STO(111) [11 $\bar{2}$ ] and BNO (0001) [10 $\bar{1}$ 0]||STO(111) [11 $\bar{2}$ ] for *a*-axis and *c*-axis texture, respectively. We found that the preferential formation of *a*-axis texture is due to the smaller lattice mismatch with STO substrate. Our DFT calculations confirm that *a*-axis texture is energetically favorable over the competing *c*-axis texture and demonstrate that the *a*-axis texture prevalence stems from its better match to the in-plane lattice parameters of the STO substrate and, therefore, lower energy penalty associated with the lattice mismatch. Spectroscopy data demonstrate that the Ni valence in BNO films is a mixture of Ni<sup>2+</sup>, Ni<sup>3+</sup>, and Ni<sup>4+</sup> oxidation states with Ni<sup>4+</sup> being dominant. STEM measurements demonstrate that NiO secondary phase formation (which contributes to the Ni<sup>2+</sup> feature) occurs close to the interface and an interfacial transition region exists at the BNO/STO interface. EELS measurements reveal the interfacial transition region is ~ 9 u.c. thick and the composition changes from Sr<sub>1-x</sub>Ba<sub>x</sub>TiO<sub>3</sub> (close to the substrate) to BaTi<sub>1-y</sub>Ni<sub>y</sub>O<sub>3</sub> (close to the BNO film). These results highlight the possibility of stabilizing Ni<sup>4+</sup> valence state in thick oxide thin films, which will offer a good platform to investigate the effects of high Ni valence on electrocatalytic performance.

## Acknowledgements

This work was supported by the U.S. Department of Energy (DOE), Office of Science, Basic Energy Sciences, Division of Materials Sciences and Engineering, Synthesis and Processing Science Program, under Award #10122. Ni *L*-edge and O *K*-edge XAS measurements were performed at the Advanced Light Source of Lawrence Berkeley National Laboratory, which is supported by the Director, Office of Science, Office of Basic Energy Sciences, U.S. Department of Energy under contract no. DE-AC02-05CH11231. Ni *K*-edge XAS measurements were performed at the Advanced Photon Source, a U.S. DOE Office of Science User Facility operated by Argonne National Laboratory under contract DE-AC02-06CH11357. This research used resources of the National Energy Research Scientific Computing Center; a DOE Office of Science User Facility supported by the Office of Science of the U.S. Department of Energy under Contract No. DE-AC02-05CH11231 using NERSC award BES-ERCAP0024614.

### Competing interests

Authors declare no conflict of interests.

### References

- [1] G. Catalan, *Phase Transitions* **81**, 729 (2008).
- [2] S. Middey, J. Chakhalian, P. Mahadevan, J. W. Freeland, A. J. Millis, and D. D. Sarma, *Annu. Rev. Mater. Res.* **46**, 305 (2016).
- [3] V. Bisogni, S. Catalano, R. J. Green, M. Gibert, R. Scherwitzl, Y. Huang, V. N. Strocov, P. Zubko, S. Balandeh, J.-M. Triscone, G. Sawatzky, and T. Schmitt, *Nat Commun* **7**, 13017 (2016).
- [4] J. Torrance, P. Lacorre, A. Nazzal, E. Ansaldo, and Ch. Niedermayer, *Phys. Rev. B* **45**, 8209 (1992).
- [5] J. A. Alonso, J. L. García-Muñoz, M. T. Fernández-Díaz, M. A. G. Aranda, M. J. Martínez-Lope, and M. T. Casais, *Phys. Rev. Lett.* **82**, 3871 (1999).
- [6] J. L. García-Muñoz, J. Rodríguez-Carvajal, and P. Lacorre, *Europhys. Lett.* **20**, 241 (1992).
- [7] J. Shi, Y. Zhou, and S. Ramanathan, *Nat Commun* **5**, 4860 (2014).
- [8] L. Wang, S. Dash, L. Chang, L. You, Y. Feng, X. He, K. Jin, Y. Zhou, H. G. Ong, P. Ren, S. Wang, L. Chen, and J. Wang, *ACS Appl. Mater. Interfaces* **8**, 9769 (2016).

- [9] S. Catalano, M. Gibert, J. Fowlie, J. Íñiguez, J.-M. Triscone, and J. Kreisel, *Rep. Prog. Phys.* **81**, 046501 (2018).
- [10] G. A. Pan, D. Ferenc Segedin, H. LaBollita, Q. Song, E. M. Nica, B. H. Goodge, A. T. Pierce, S. Doyle, S. Novakov, D. Córdova Carrizales, A. T. N'Diaye, P. Shafer, H. Paik, J. T. Heron, J. A. Mason, A. Yacoby, L. F. Kourkoutis, O. Erten, C. M. Brooks, A. S. Botana, and J. A. Mundy, *Nat. Mater.* **21**, 160 (2022).
- [11] D. Li, K. Lee, B. Y. Wang, M. Osada, S. Crossley, H. R. Lee, Y. Cui, Y. Hikita, and H. Y. Hwang, *Nature* **572**, 624 (2019).
- [12] M. Osada, B. Y. Wang, B. H. Goodge, K. Lee, H. Yoon, K. Sakuma, D. Li, M. Miura, L. F. Kourkoutis, and H. Y. Hwang, *Nano Lett.* **20**, 5735 (2020).
- [13] S. Zeng, C. Li, L. E. Chow, Y. Cao, Z. Zhang, C. S. Tang, X. Yin, Z. S. Lim, J. Hu, P. Yang, and A. Ariando, *Sci. Adv.* **8**, eab19927 (2022).
- [14] D. Ferenc Segedin, B. H. Goodge, G. A. Pan, Q. Song, H. LaBollita, M.-C. Jung, H. El-Sherif, S. Doyle, A. Turkiewicz, N. K. Taylor, J. A. Mason, A. T. N'Diaye, H. Paik, I. El Baggari, A. S. Botana, L. F. Kourkoutis, C. M. Brooks, and J. A. Mundy, *Nat. Commun.* **14**, 1468 (2023).
- [15] Q. Li, C. He, J. Si, X. Zhu, Y. Zhang, and H.-H. Wen, *Commun Mater* **1**, 16 (2020).
- [16] P. Puphal, Y.-M. Wu, K. Fürsich, H. Lee, M. Pakdaman, J. A. N. Bruin, J. Nuss, Y. E. Suyolcu, P. A. van Aken, B. Keimer, M. Isobe, and M. Hepting, *Sci. Adv.* **7**, eab18091 (2021).
- [17] L. Wang, K. A. Stoerzinger, L. Chang, J. Zhao, Y. Li, C. S. Tang, X. Yin, M. E. Bowden, Z. Yang, H. Guo, L. You, R. Guo, J. Wang, K. Ibrahim, J. Chen, A. Rusydi, J. Wang, S. A. Chambers, and Y. Du, *Adv. Funct. Mater.* **28**, 1803712 (2018).
- [18] J. G. Lee, J. Hwang, H. J. Hwang, O. S. Jeon, J. Jang, O. Kwon, Y. Lee, B. Han, and Y.-G. Shul, *J. Am. Chem. Soc.* **138**, 3541 (2016).
- [19] N. Li, D. K. Bediako, R. G. Hadt, D. Hayes, T. J. Kempa, F. von Cube, D. C. Bell, L. X. Chen, and D. G. Nocera, *Proc. Natl. Acad. Sci. U.S.A.* **114**, 1486 (2017).
- [20] B. Weng, Z. Song, R. Zhu, Q. Yan, Q. Sun, C. G. Grice, Y. Yan, and W.-J. Yin, *Nat Commun* **11**, 3513 (2020).
- [21] J. Zaanen, G. A. Sawatzky, and J. W. Allen, *Phys. Rev. Lett.* **55**, 418 (1985).
- [22] K. Lee, B. H. Goodge, D. Li, M. Osada, B. Y. Wang, Y. Cui, L. F. Kourkoutis, and H. Y. Hwang, *APL Materials* **8**, 041107 (2020).
- [23] J. Liu, E. Jia, L. Wang, K. A. Stoerzinger, H. Zhou, C. S. Tang, X. Yin, X. He, E. Bousquet, M. E. Bowden, A. T. S. Wee, S. A. Chambers, and Y. Du, *Adv. Sci.* **6**, 1901073 (2019).
- [24] S. Zeng, C. S. Tang, X. Yin, C. Li, M. Li, Z. Huang, J. Hu, W. Liu, G. J. Omar, H. Jani, Z. S. Lim, K. Han, D. Wan, P. Yang, S. J. Pennycook, A. T. S. Wee, and A. Ariando, *Phys. Rev. Lett.* **125**, 147003 (2020).
- [25] Y. Li, W. Sun, J. Yang, X. Cai, W. Guo, Z. Gu, Y. Zhu, and Y. Nie, *Front. Phys.* **9**, 719534 (2021).
- [26] L. Wang, Z. Yang, X. Yin, S. D. Taylor, X. He, C. S. Tang, M. E. Bowden, J. Zhao, J. Wang, J. Liu, D. E. Perea, L. Wangoh, A. T. S. Wee, H. Zhou, S. A. Chambers, and Y. Du, *Sci. Adv.* **7**, eabe2866 (2021).
- [27] L. Wang, Z. Yang, M. E. Bowden, J. W. Freeland, P. V. Sushko, S. R. Spurgeon, B. Matthews, W. S. Samarakoon, H. Zhou, Z. Feng, M. H. Engelhard, Y. Du, and S. A. Chambers, *Adv. Mater.* **32**, 2005003 (2020).

- [28] L. Wang, J. Zhao, C.-T. Kuo, B. E. Matthews, M. T. Oostrom, S. R. Spurgeon, Z. Yang, M. E. Bowden, L. W. Wangoh, S.-J. Lee, J.-S. Lee, E.-J. Guo, J. Wang, S. A. Chambers, and Y. Du, *Phys. Rev. Materials* **6**, 075006 (2022).
- [29] E. Cho, K. Klyukin, S. Ning, J. Li, R. Comin, R. J. Green, B. Yildiz, and C. A. Ross, *Phys. Rev. Materials* **5**, 094413 (2021).
- [30] F. Calle-Vallejo, J. I. Martínez, J. M. García-Lastra, M. Mogensen, and J. Rossmeisl, *Angewandte Chemie International Edition* **49**, 7699 (2010).
- [31] M. Zinkevich, *Journal of Solid State Chemistry* **178**, 2818 (2005).
- [32] Y. Takeda, T. Hashino, H. Miyamoto, F. Kanamaru, S. Kume, and M. Koizumi, *Journal of Inorganic and Nuclear Chemistry* **34**, 1599 (1972).
- [33] R. Gottschall, R. Schöllhorn, M. Muhler, N. Jansen, D. Walcher, and P. Gütllich, *Inorg. Chem.* **37**, 1513 (1998).
- [34] J. J. Lander, *Acta Cryst* **4**, 148 (1951).
- [35] A. M. Arévalo-López, M. Huvé, P. Simon, and O. Mentré, *Chem. Commun.* **55**, 3717 (2019).
- [36] M. Retuerto, F. Calle-Vallejo, L. Pascual, P. Ferrer, Á. García, J. Torrero, D. Gianolio, J. L. G. Fierro, M. A. Peña, J. A. Alonso, and S. Rojas, *Journal of Power Sources* **404**, 56 (2018).
- [37] J. G. Lee, H. J. Hwang, O. Kwon, O. S. Jeon, J. Jang, and Y.-G. Shul, *Chem. Commun.* **52**, 10731 (2016).
- [38] J. J. Lander and L. A. Wooten, *J. Am. Chem. Soc.* **73**, 2452 (1951).
- [39] A. Biswas, C.-H. Yang, R. Ramesh, and Y. H. Jeong, *Prog. Surf. Sci.* **92**, 117 (2017).
- [40] P. C. Rogge, R. U. Chandrasena, A. Cammarata, R. J. Green, P. Shafer, B. M. Lefler, A. Huon, A. Arab, E. Arenholz, H. N. Lee, T.-L. Lee, S. Nemšák, J. M. Rondinelli, A. X. Gray, and S. J. May, *Phys. Rev. Materials* **2**, 015002 (2018).
- [41] L. Wang, Y. Du, P. V. Sushko, M. E. Bowden, K. A. Stoerzinger, S. M. Heald, M. D. Scafetta, T. C. Kaspar, and S. A. Chambers, *Phys. Rev. Materials* **3**, 025401 (2019).
- [42] R. Qiao, L. A. Wray, J.-H. Kim, N. P. W. Pieczonka, S. J. Harris, and W. Yang, *J. Phys. Chem. C* **119**, 27228 (2015).
- [43] G. Greczynski and L. Hultman, *Journal of Applied Physics* **132**, 011101 (2022).
- [44] W.-S. Yoon, M. Balasubramanian, K. Y. Chung, X.-Q. Yang, J. McBreen, C. P. Grey, and D. A. Fischer, *J. Am. Chem. Soc.* **127**, 17479 (2005).
- [45] S. Roychoudhury, R. Qiao, Z. Zhuo, Q. Li, Y. Lyu, J. Kim, J. Liu, E. Lee, B. J. Polzin, J. Guo, S. Yan, Y. Hu, H. Li, D. Prendergast, and W. Yang, *Energy Environ. Mater.* **4**, 246 (2021).

## Figures and Figure Captions

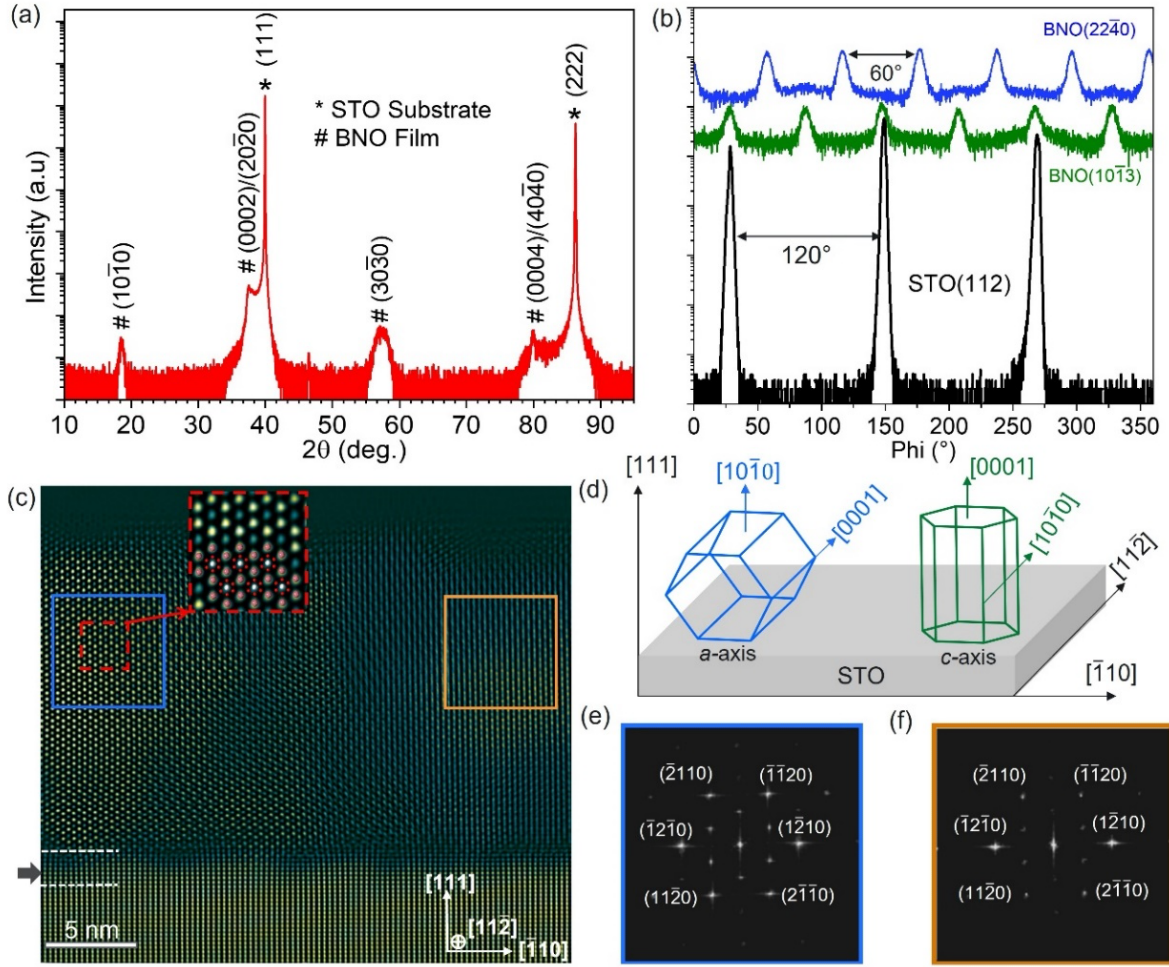


**Figure 1.** Synthesis of epitaxial hexagonal BNO film on STO(111) and structural characterization. (a) High resolution XRD  $\theta$ - $2\theta$  scan showing the presence of  $a$ - and  $c$ -axis mixed textures. (b) Phi-scans along two different planes demonstrating two distinct epitaxial relationships. (c) STEM-HAADF image viewed along STO  $\langle 11\bar{2} \rangle$  zone axis, highlighting two ‘different’ lattice structures in the selected regions. The hexagonal structure of BNO (pink spheres, Ba; white spheres, Ni; red spheres, O) is overlaid for comparison. The black arrow denotes the interfacial transition layer. (d) Schematics illustrating the epitaxial relationships of the two textures on STO(111). (e) and (f) Fast Fourier transforms of the two selected regions in (c), revealing the corresponding reciprocal space information.

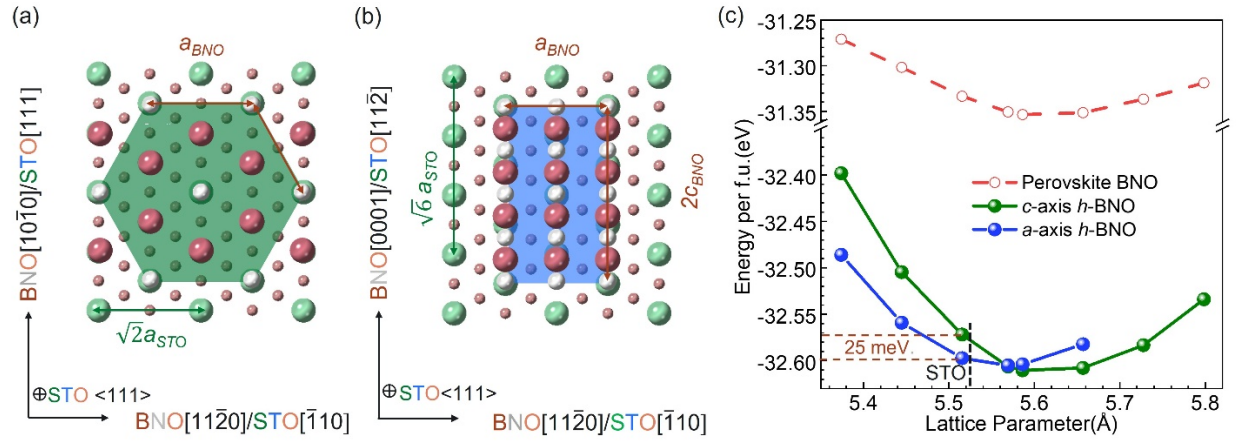


**Figure 2.** Crystal structures and corresponding BNO potential energy for the film/substrate orientations for two *h*-BNO textures viewed down the STO<111> zone axis. (a) Crystal structure of the *c*-axis texture with an epitaxial relationship of BNO(0001)  $[10\bar{1}0]\parallel$ STO(111)  $[11\bar{2}]$  and (b) *a*-axis texture with an epitaxial relationship of BNO( $10\bar{1}0$ )  $[0001]\parallel$ STO( $11\bar{2}$ )  $[111]$ . (c) Energy per formula unit (f.u.) vs substrate lattice parameter for the two textures of *h*-BNO and the perovskite BNO phase supported on cubic substrates.

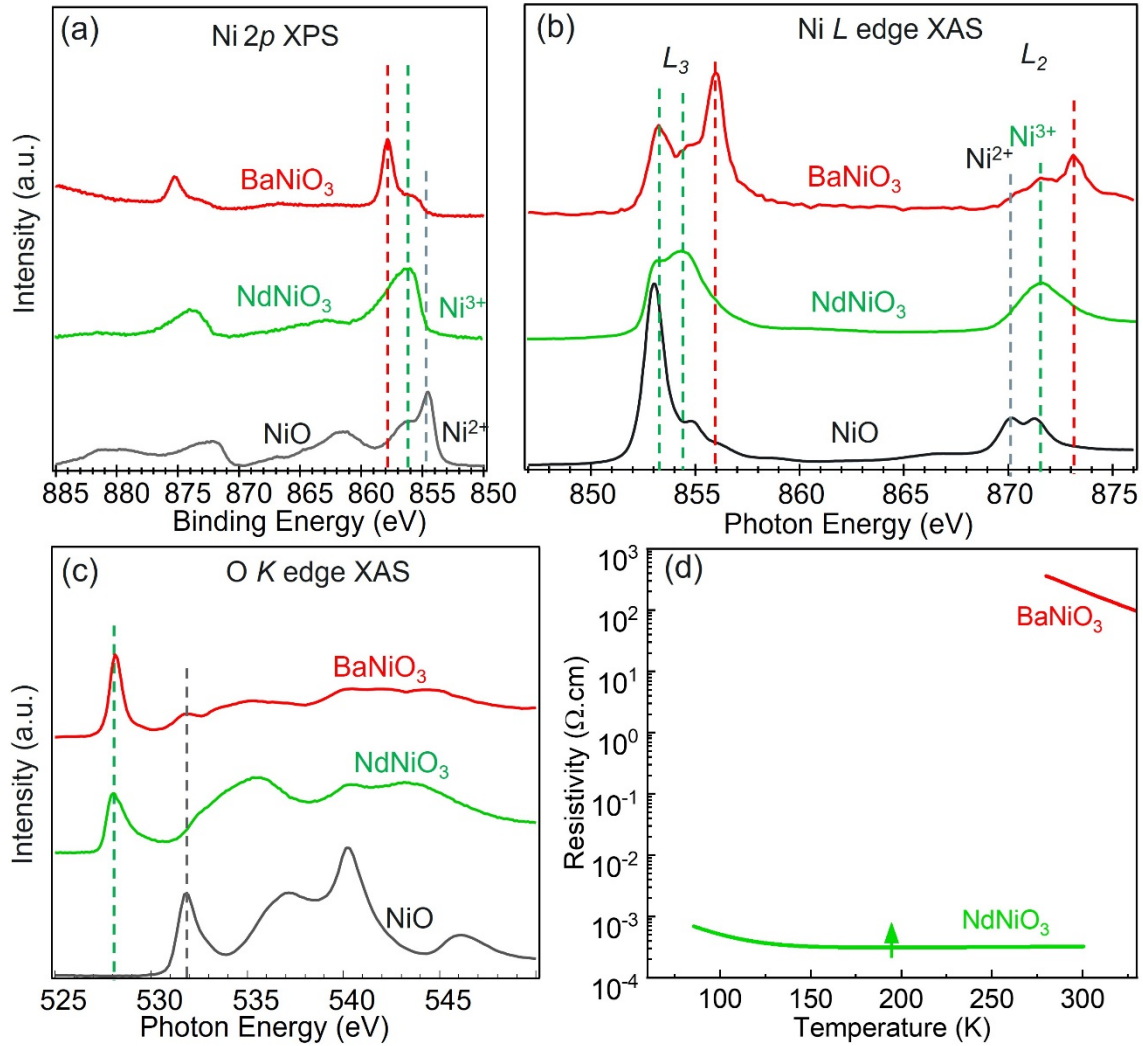


**Figure 3.** Spectroscopy data and in-plane transport behavior. (a) In situ Ni 2p XPS. The Ni 2p<sub>2/3</sub> peak position were marked by dashed lines. (b) Ni L-edge XAS. The Ni L<sub>2</sub> edge peak position for BNO, NdNiO<sub>3</sub>, and NiO was marked by red, green, and grey dashed lines, respectively. (c) O K-edge XAS. The O K pre-edge position for NdNiO<sub>3</sub> and NiO was marked by green and grey dashed lines, respectively. (d) Temperature-dependent resistivity of BaNiO<sub>3</sub> and NdNiO<sub>3</sub>. The green arrow denotes the metal-insulator transition temperature for NdNiO<sub>3</sub>.